Reviewed Preprint
v1 • June 16, 2026
Not revised

For correspondence:
golding@austin.utexas.edu

* Equal contributions

Competing interests: No competing interests declared

Funding: See page 15

Reviewing editor: Catherine Emily Carr, University of Maryland, United States

Dendritic delay lines shape the computation of sound location in neurons of the gerbil medial superior olive

Jared Casarez[1,*], Rebecca I Voglewede[1,*], Bradley D Winters[2,3], Ken Ledford[1], Nace L Golding[1]

[1]The University of Texas at Austin, Department of Neuroscience and Center for Learning and Memory, Austin, United States • [2]Department of Biological Sciences and University Hospitals – NEOMED Hearing Research Center, Northeast Ohio Medical University, Rootstown, United States • [3]Brain Health Research Institute, Kent State University, Kent, United States

eLife Assessment

This is a **fundamental** study that clarifies the cellular mechanism of sound localization in the horizontal plane. The analysis of medial superior olivary neurons provides experimental and computational evidence for a new mechanism in which a range of asymmetric dendritic delays permits individual MSO neurons to represent the full range of biologically relevant ITDs. Using elegant 2-photon guided simultaneous recordings from distal dendrites and soma, along with compartmental modeling on anatomically reconstructed neurons, the authors provide **compelling** evidence that this mechanism contributes to microsecond-level tuning.

https://doi.org/10.7554/eLife.111364.1.sa4

Abstract

In mammals, neurons of the medial superior olive encode information about sounds arising from discrete spatial locations along the horizon. This tuning requires that an internal delay in the brain must offset acoustic disparities to ensure coincident arrival of excitatory inputs driven from the two ears. The source of this optimal internal delay, originally assumed to arise from axonal delay lines, is currently controversial in mammals. Here we use 2-photon guided paired dendritic and somatic recordings together with compartmental modeling of 40 complete MSO neuron morphologies to demonstrate that the dendrites themselves serve as a significant source of internal delay. We show that most MSO neurons exhibit morphological asymmetries that impose different EPSP delays across dendrites and shifts in optimal interaural time differences. Dendrite-based delays in the mammalian MSO are heterogeneous within each isofrequency laminae and provide a stable, structural mechanism to help tune individual neurons to sounds from different azimuthal locations.

Introduction

Spatial information in the auditory system is critical for humans and other mammals to assemble a 3-dimensional view of the world as well as to understand speech and communication signals, especially in environments with many sounds overlapping in time and in frequency. The auditory system is distinct from vision or touch in that there is no explicit peripheral representation of space, in this case in the cochlea, only a representation of frequency. Accordingly, the central auditory system must compute horizontal sound location indirectly by combining a series of monaural and binaural cues [1,2]. Spatial coding in the central auditory system is a prime example of a centrally synthesized or computational map.

Interaural time difference cues are used by birds and mammals to compute horizontal sound location at low frequencies [3]. In mammals this computation takes place in the medial superior olive (MSO), whose neurons are the first to receive converging excitatory and inhibitory inputs driven from the two ears. Intriguingly, in individual neurons, binaural inputs are integrated within a bipolar dendritic architecture, with ipsilateral and contralateral excitatory inputs segregated onto lateral and medial dendritic branches respectively [4,5]. Ipsilateral and contralateral inhibition converges onto the soma and proximal dendrites [4–8]. MSO neurons detect the optimal combination of these inputs, converting temporal coincidence into a rate code [6,9,10].

The concept of internal delay is central to coincidence detection in the MSO, where acoustic delays to the two ears are countered in time by a mechanism of delay inside the brain. This internal temporal asymmetry was postulated in early models to arise from axonal delay lines formed by ladder-like combinations of bilateral excitatory inputs (the "Jeffress model") [11]. While the Jeffress model enjoys strong support in birds [12–14], comparable studies in mammals have failed to reveal systematic axonal input delay lines nor any mapping of delay along the nucleus [6,15,16]. More recently, there is evidence that fast inhibition mediates internal delay by shifting the peaks of EPSPs [17–19]. However, this mechanism is subject to vigorous debate [20–22], and it is not clear that this mechanism alone can explain the range of receptive field locations in the MSO or their insensitivity to sound level. Other mechanisms have been proposed to mediate internal binaural asymmetry, including asymmetrical axon position, medio-lateral differences in the rising slopes of EPSPs [23], and differences in tuning of binaural inputs ("stereausis") [24,25].

All models of coincidence detection must address the issue of the temporal distortions imposed by the dendrites themselves. However, to date models of MSO neurons have been represented either as point neurons or as simplified, symmetrical "ball-and-stick" models [17,26–30]. Previous measurements of dendritic propagation have revealed that EPSPs encounter delays in their propagation to the soma up to ~150 μs, despite some degree of temporal compensation by activation of low voltage-activated K channels in the soma and proximal dendrites [27]. However, these measurements have largely been restricted to the proximal half of the dendritic arbor and have relied on averaging highly variable populations of neurons. Given that the dendrites of MSO neurons alter their branching pattern and diameters during early hearing and following disruptions of normal hearing [31–33], they might serve as a potential mechanism for adjusting the timing requirements for sounds from the two ears to arrive coincidently at the soma and axon.

Here we demonstrate that the dendritic arbors of MSO neurons are highly heterogeneous and show a striking continuum of asymmetry across the medial and lateral branches that receive segregated inputs driven respectively from the two ears. We show with dual 2-photon fluorescence-guided patch recordings that inputs to smaller and/or more distal dendrites show more substantial propagation delays than previously recognized, and computational modeling of a large population of intact neuronal morphologies shows that these dendritic asymmetries translate into stable internal delays that, as a population, could account for the full range of naturally occurring horizontal locations. Finally, we show that inhibition preserves the effects of dendritic asymmetry on interaural time differences (ITDs) and helps bring the region of maximum slope of firing changes within the ecologically relevant range. Thus dendrite-based delay lines likely work synergistically with other integrative mechanisms purported to shape the perception of horizontal position in mammals.

Results

To understand how MSO neurons process interaural time differences in the dendrites, we made fluorescence-guided dendritic and somatic patch-clamp recordings visualized under 2-photon microscopy. Using this approach, we were able to target the distal third of the dendritic arbor, including secondary and tertiary branches, regions that have largely escaped investigation in these neurons. We then injected simulated EPSCs (τ_{rise} and τ_{decay}, 0.2 ms) into the dendritic pipette and recorded potentials simultaneously at both dendrites and soma. We observed strong variability in both the percent amplitude attenuation at the soma $\left(\left(\frac{V_{soma}}{V_{dend}}\right) \times 100\right)$ as well as the propagation delay of the EPSP, measured as the difference in EPSP peak time at the soma relative

to the dendrite (Fig. 1). Notably, the delays measured in these recordings ranged between 100 and 300 μs, exceeding the physiological range of ITDs measured in gerbils. In these recordings, there was little correlation between local morphological features of recorded dendrites and propagation delay of the EPSP, measured as the difference in the peak timing of dendritic and somatic EPSPs (Fig. 2a-c). However, there was a stronger correlation between the local dendritic membrane time constant and EPSP propagation delay (Fig. 2d). In addition, there was a weak trend of increasing dendritic membrane time constant with recording distance (Fig. 2e), possibly because of proximity to the dendritic terminations. These results may reflect that an understanding of the integrative properties of the dendrites requires an analysis of the larger morphological and electrotonic structure of the neuron.

To understand how overall dendritic structure impacts binaural coincidence detection, we analyzed a database of biocytin-filled MSO neurons that exhibited complete dendritic structures (40 of 270 neurons from Bondy et al., 2021 [34]; Fig. 3). We quantified dendritic length, surface area and branching, with special emphasis on comparisons of medial and lateral dendritic arbors. Higher-order (2° and higher) dendritic branches were prominent in these neurons, comprising 70% of the membrane surface area (Fig. S1).

A striking feature of most neurons in this data set was an overall asymmetry between the lateral and medial dendritic arbors, reflecting differences in length, branching, and/or diameter of the dendrites (Fig. 3a-c). We quantified this asymmetry according to two parameters, the average path length (average length from each dendritic end to the soma) and membrane surface area, with the latter parameter reflecting the collective influence of dendritic length, diameter and branching pattern. We then defined the degree of bilateral asymmetry as fold differences between the larger vs. smaller dendritic measure for each parameter. We observed no obvious correlation between dendritic asymmetry and tonotopic location (Fig. 3a, left and 3b, top). However, we found that dendritic asymmetry formed a finely graded continuum, with a slight bias toward lateral dendrites (Fig. 3b, bottom). Interestingly, there were no significant differences in population averages of the medio-lateral path length and surface area (1.080 ± 0.057 and 1.112 ± 0.133 fold differences; p=0.562), though there was a slight lateral bias. These results indicate that the averaging of dendritic morphological parameters across neurons obscures what is likely a key structural and computational feature.

To understand how morphological asymmetry impacts synaptic integration, we constructed compartmental models using the same 40 reconstructions analyzed in Fig. 3. We introduced an excitatory synaptic conductance (alpha function: τ = 290 μs) into each dendritic compartment and then measured the voltage attenuation and propagation delay from the dendritic input location to the soma (Figs. 4-5). At comparable distances from the soma, EPSP amplitude at the site of synaptic input and following propagation to the soma varied considerably, like the physiological data from paired recordings in Figure 1 (Fig. 4a). Plots of local dendritic and propagated somatic EPSP amplitudes across all synapse locations further revealed striking asymmetries in propagation efficacy of EPSPs to the soma (Fig. 4b, “Active cell”). In MSO neurons, the timing and attenuation of EPSPs along dendrites are influenced both by passive cable filtering as well as interactions with low voltage-activated K channels, which are active in the subthreshold voltage range in these neurons [27]. To determine the degree to which asymmetries in low voltage-activated K channels impact EPSP attenuation at the soma we converted all voltage-activated conductances to leak channels (Fig. 4b, “Passive cell”; see Methods). While EPSPs propagated slightly more effectively to the soma from all dendritic locations in the passive model, it did not fundamentally disrupt mediolateral asymmetry, indicating that these differences arose primarily from the passive electrotonic architecture of the cell. The branching structure had a significant effect on dendritic propagation asymmetry. This could be better visualized in inward morphoelectrotonic transforms of cells, which exhibits dendritic compartments according to their electrotonic, versus physical lengths. In the example neuron in Fig. 4c, large primary dendrites are deemphasized, while thinner secondary and tertiary branches appear as electrotonically elongated. Differences between the medial and lateral dendritic arbors in this neuron and many others gave rise to asymmetries in the magnitude of the average EPSP arriving at the soma.

Fig. 1. Heterogeneity in attenuation and timing of simulated excitatory synaptic potentials following propagation from distal dendritic locations to the soma.

a,b, 2-photon fluorescence-guided dual dendritic and somatic patch recordings from two MSO neurons of comparable distances (78 and 73 µm, respectively). Example neuron in $\mathbf{a_1}$ shows stronger attenuation of somatic propagation of a simulated EPSP ($\mathbf{a_2}$ vs. $\mathbf{b_2}$) and longer peak delay ($\mathbf{a_3}$ vs. $\mathbf{b_3}$). EPSC amplitudes: cell **a**, 600 pA; cell **b**, 400 pA. **c,d**, Group data for attenuation and peak delay for all paired MSO neuron recordings. There is a poor correlation of both measures as a function of distance.

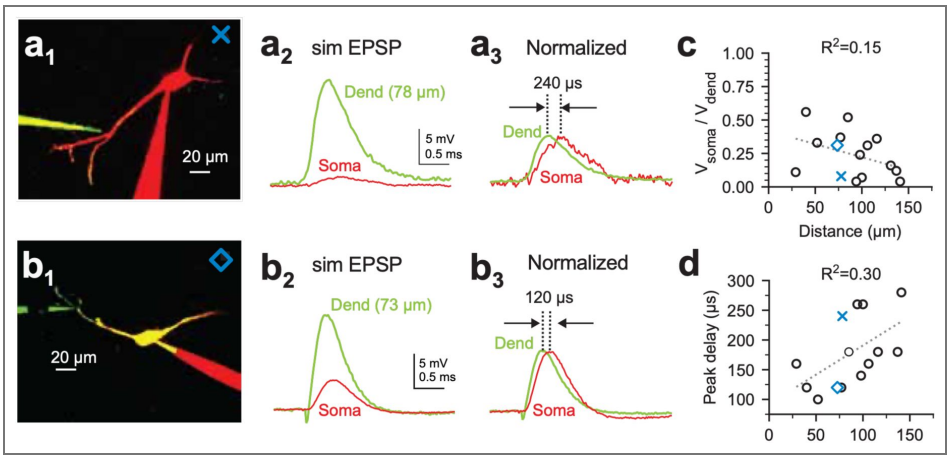

Fig. 2. EPSP propagation delays are not correlated with local morphology but rather more global physiological properties.

a, Closeups of distal dendritic morphology during paired dendritic and somatic recordings. **b,c**, Delay of peak EPSPs during propagation from dendrite to soma shows no significant correlation with local diameter or tapering rate of local dendrite. (dendritic EPSCs: 400-1000 pA). **d**, Peak EPSP delay from dendrite to soma was weakly correlated with the membrane time constant recorded at the dendritic recording site. **e**, Dendritic membrane time constant increased with distance of the recording site from the soma.

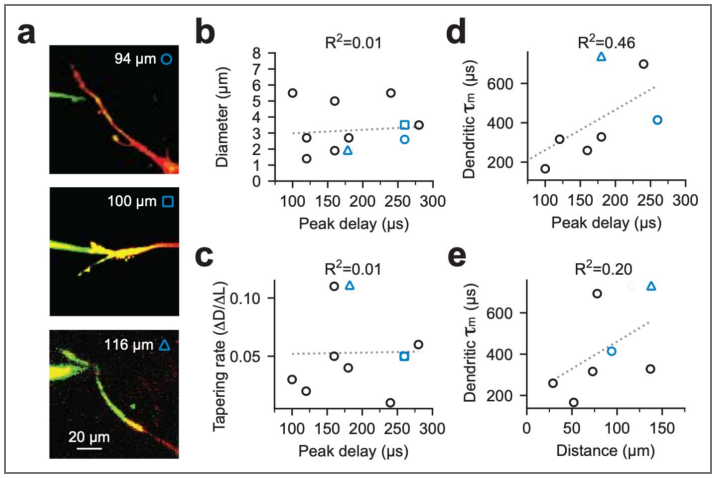

Fig. 3. MSO neuron morphology is inhomogeneous and asymmetric, regardless of tonotopy.

a, Reconstructed morphologies rank ordered by tonotopy (left) and degree of asymmetry (right; average path length). Orderings span from low frequency (top) to high frequency (bottom) and medial (top) and lateral (bottom) asymmetry, respectively. Colored gradients added to visualize ordering. Uniquely colored dots placed beneath each morphology for differentiation. **b**, Fold difference between average path length of medial and lateral dendrites for all reconstructed morphologies (n=40) with vertical axes ordered by tonotopic location (top) or degree of asymmetry (bottom). Gradients added as in **a**. Colored points correspond to **a**. **c**, Same as **b**, except comparing total surface area of medial and lateral branches. Average medio-lateral path length and surface area fold differences (± SEM) were 1.080 ± 0.057 and 1.112 ± 0.133 (biased laterally) and tonotopic R^2 values were -0.42 and -0.23.

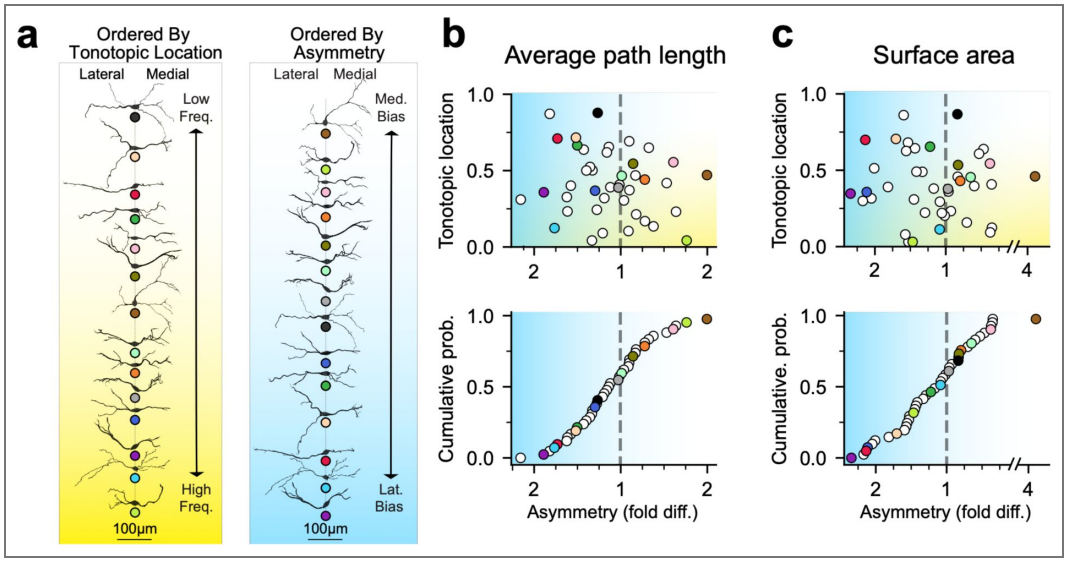

Fig. 4. MSO morphology nonlinearly filters and attenuates propagating EPSPs through its passive cable properties.

a, Visualization EPSP filtering at different dendritic sites. Cell morphology (top) with similarly distant example synaptic sites indicated with green circles and corresponding numbers. Red triangle indicates the somatic compartment. Synaptic conductance indicated as g_{syn}. Four sets of paired dendritic (green) and somatic (red) traces (bottom) for each example synaptic site. Numbering of traces corresponds to labels on morphology above. Dendritic distance from soma for each site indicated below traces. **b**: Same procedure as in **a**, with an adjusted unitary synaptic conductance (see Methods), with measurements from each computational compartment. Model morphology and orientation same as in **a**. Comparison between active channel (left) and passive channel model (right). Recorded EPSP amplitude at synaptic (top, green) and somatic (bottom, red) compartment as a function of distance from soma. **c**, Actual (top) and electrotonically transformed (bottom) morphologies. Transformation visualizes degree of EPSP attenuation from each compartment (see Methods). **d**, Group data (n=40) of average somatic depolarization asymmetry between mediolateral sides. Gradient as in Fig 3. Dotted line indicates equal medial and lateral average somatic depolarizations. Cell from **a-c** indicated with a triangle.

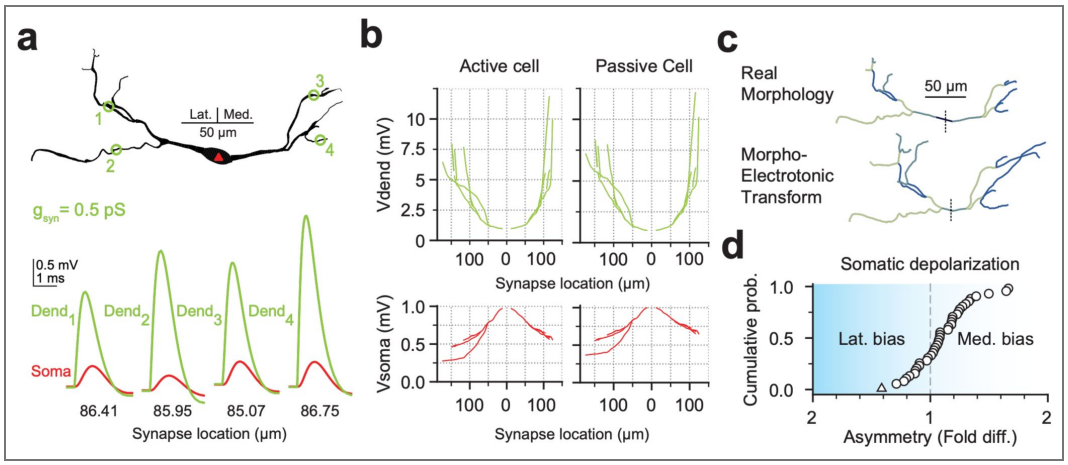

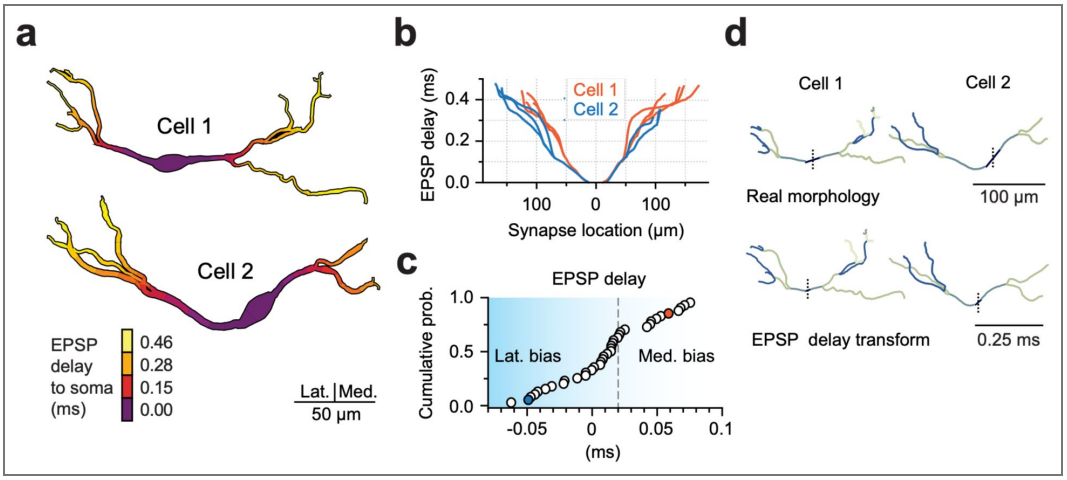

Fig. 5. EPSP timing significantly varies within and between cells, with morphological asymmetry informing overall cell timing.

a, EPSP delay visualization in two exemplar MSO neurons. Coloring of each cell corresponds to the propagation delay of EPSPs to the soma from its respective compartment. Legend of propagation delay coloring in top right. Cells are oriented mediolaterally according to the scale bar. Outline added to increase gradient readability. **b**, Same data as in **a**, except as a function of distance from the soma. Orientation of cells same as in **a**. **c**, Group data (n=40) of the difference in average EPSP propagation delay between medial and lateral dendrites. Cells 1 & 2 are indicated with same color as in **b**. Dotted line at 0 ms indicates an equal average EPSP delay between sides. Blue gradient along horizontal axis (as in Fig. 3) to indicate spectrum of asymmetry. **d**, Morphological transforms according to EPSP delays. Morphological centroids of actual cell morphologies (top) and transformed morphologies (bottom). Length corresponds to each sections EPSP delay contribution. Coloring of cell sections is consistent between actual and transformed morphologies for easier differentiation and comparison. Dotted line added to mark the midline.

Further, we observed that our population of cells formed a continuum in the degree of somatic depolarization asymmetry, in line with the asymmetry in dendritic structure (Fig. 4d). Dendritic asymmetry also translated into differences in average EPSP timing across the medial and lateral dendrites. Figure 5a shows for two example neurons the spatial profile of delays of EPSPs propagating from each dendritic compartment to the soma. The asymmetry in dendritic timing can be more quantitatively visualized in plots of peak EPSP delay ($t_{dend} - t_{soma}$) as a function of dendritic distance from the soma (Fig. 5b). Dendritic branch points often introduced substantial jumps in propagation delays, and this is reflected in these plots as increases in slope. To quantify the influence of dendritic asymmetry on the optimal summation of bilateral EPSPs at the soma, we measured the electrotonic delay at the soma for every 2 μm compartment of lateral and medial dendritic subtrees. In our population of 40 neuron models, there were differences in the average relative time of arrival of EPSPs to the soma from compartments in the medial and lateral dendrites. Further, these differences formed a smoothly graded continuum of delays (Fig. 5c).

MSO neurons exhibit a range of intrinsic electrical properties, and so we examined a subset of neuron morphologies to understand the functional implications of this physiological diversity. Using a neuron with an asymmetric dendritic arbor, we systematically slowed the membrane time constant by reducing the density of both low voltage-activated K channels and HCN channels (Fig. S2). In both cases, the timing of EPSPs reaching the soma was linearly related to the value of the membrane time constant. Thus, the effects of dendritic asymmetry on EPSP timing and amplitude at the soma are expected to be substantially higher in MSO neurons with slower intrinsic membrane properties. To understand how the differential timing of EPSPs propagating from medial and lateral dendrites is translated into ITDs, we simulated binaural excitatory input using a spiking model of MSO neurons (see Methods). This model featured one axonal input per terminal branch segment as well as a centripetal (dendrite-to-soma) pattern of dendritic innervation, running from the terminal compartments to the soma, in accordance with results from anatomical studies (Fig. 6a) [15,16,28]. The conduction velocity of these inputs was set to 1 ms^{-1}, approximating values of unmyelinated terminal axonal arborizations of similar caliber [13,35]. The timing of ipsilateral and contralateral inputs was varied systematically, triggering spiking only when the two inputs were in close coincidence (Fig. 6b). The location of these excitatory ITD functions were dependent on medio-lateral asymmetry. Functions shifted toward the side of the electrically longer dendrite, reflecting the need for earlier activation of that side to compensate for a longer dendritic propagation delay (Fig. 6c). Our population of 40 neurons showed peak firing at delays that traversed a continuum of values (-0.11 to 0.08 ms, median -0.02; Fig. 6d; Fig. S3). The precise range of values depended in part on the assumptions on the velocity of excitatory axons. The largest range of ITDs was achieved when there was closer matching between the velocity of axonal input velocity and postsynaptic EPSPs propagating from the dendrites to the soma, which maximized temporal coincidence at the soma of spatially disparate inputs in the dendrites (Fig. 6e). Finally, ITDs shifted less than 3% in the face of input amplitude changes that resulted in firing probabilities between 0.2 and 0.8, indicating that dendritic asymmetry is highly stable across changing stimulus conditions.

Inhibition is a critical component of ITD encoding, although its precise role is subject to vigorous debate. To understand how dendritic asymmetry impacts the effects of inhibition, we added bilateral inhibitory conductances to the somatic compartment of the bilateral excitatory model in Fig. 6, consistent with the known somatically biased innervation of MSO neurons from the lateral and medial nuclei of the trapezoid body (LNTB and MNTB; [8,36]). We set the timing of inhibitory conductances to be 500 μs in advance of excitatory inputs from the same side, in accordance with a previously published estimate [21]. We then adjusted the amplitude of inhibitory conductances to produce summed IPSPs of between ~1-3 mV, which reduced firing probability by 20, 40, 60 and 100% (Fig. 7a). With increasing amplitude of IPSPs, resultant ITD functions decreased in halfwidth by 57%, but the location of functions with increasing levels of inhibition were not significantly different from the model with only excitatory inputs (0.070-0.078 ms; centroid, p=0.984; group data). However, the region of maximum slope consistently shifted towards zero, in accordance with a sinking iceberg receptive field scenario (Fig. 7d; -0.27 to 0.07 ms). We then tested how the relative timing of excitatory and inhibitory inputs altered ITD

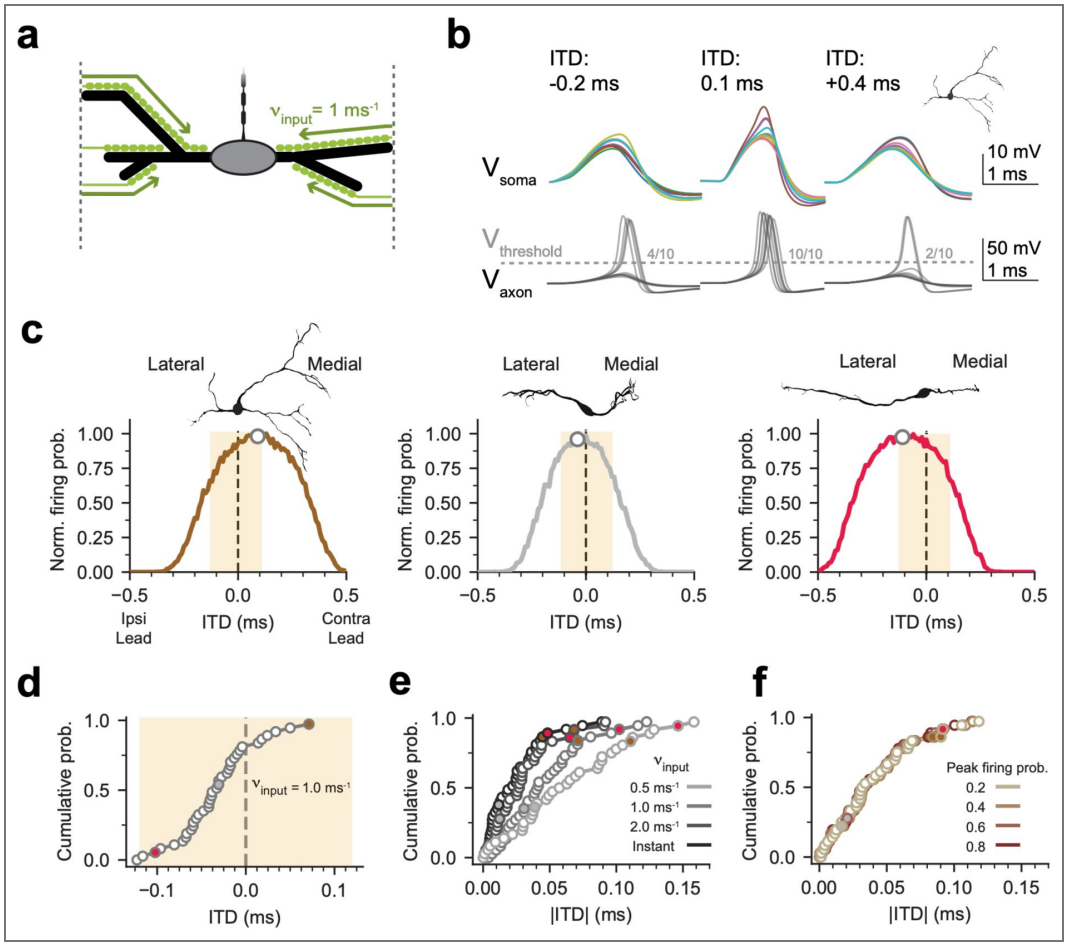

Fig. 6. Simulated ITDs demonstrate conservation of morphological impact on coincident detection.

a, Schematic visualization of ITD innervation. Somatic compartment and dendrites are shown in gray and black, respectively. Green bulbs represent excitatory synapses, with corresponding arrows to illustrate axonal input velocity (v_{input}). Dotted lines illustrate point at which there is considered to be no axonal input delay (see Methods). Axon attached to soma, with initial segment, nodes, and internodes. **b**, Example somatic (top) and axonal (bottom) traces from ITD simulations. ITDs of -0.2 ms (left), 0.1 ms (middle, optimal coincidence), 0.3 ms (right) shown. Traces colored only for differentiation. Dotted line ($V_{threshold}$) indicates depolarization threshold for action potential consideration. Morphology of model cell indicated in upper right. **c**, Three example ITD firing curves from varied morphologies, medially biased (left), symmetrical (middle), and laterally biased (right). Corresponding morphologies imaged above. Light orange span represents range of ecologically possible ITDs for model species. Dashed line placed at ITD of 0 ms. Dot indicates centroid ITD value. **d**, Sorted group data (n=39) of centroid ITDs, with v_{input} = 1 ms^{-1}. Cells from **c** indicated with filled colored points. **e,f**, Sorted group data (n=39) of absolute centroid ITDs, varying axonal input velocity (**e**) and peak firing probability (**f**). Cells from **c** indicated with correspondingly filled colored points.

functions. Varying the timing of IPSPs relative to EPSPs from –0.5 ms to 0.25 ms altered the location of ITD functions by 0.04 ms, from 0.07 to 0.11 ms. Over the population of MSO neuron morphologies, the presence of inhibition reduced firing probability without fundamentally shifting the location of ITD functions. However, the region of the function where there is maximal change in firing rate is necessarily impacted by the decrease in ITD width (Fig. S4), suggesting that dendritic asymmetry and inhibition provide separate contributions to MSO neurons' receptive field locations.

Discussion

The passive cable properties of neuronal dendrites are known to impart both attenuation and delay on EPSPs as they propagate to the soma, commensurate with the distance traversed and the anatomical features of the dendrite itself. However, the functional significance of dendritic geometry and its impact on action potential firing is often difficult to assess. Here we have newly identified a critical function for dendritic structure in the processing of sound localization cues in MSO neurons of the auditory brainstem. We have shown that the bipolar dendritic arbor of MSO neurons is typically asymmetrical, imposing a corresponding asymmetry in the relative timing required for excitatory inputs to drive optimal patterns of action potential output. Our compartmental models show that variation in dendritic morphology across cells exerts a continuum of temporal influences sufficient to shift spatial receptive fields across the full biological range of ITDs available to the gerbil. These shifts are insensitive to differences in intensity and likely work together with other sources of internal delay to enable MSO neurons to stably encode spatial locations along the horizontal plane.

Role of dendritic-based delays in the detection of input sequences

The idea that dendritic structure could dictate detection of temporal sequences of input was first explored in the pioneering computer models of Wilfred Rall. These studies showed that attenuation and propagation delays of EPSPs traveling from the dendrites to the soma could impart greater sensitivity to somatically vs distally directed activation sequences of excitatory inputs, where the longer propagation time of more distal EPSPs is compensated by their earlier activation [37]. Preferential firing to centripetal (distal to proximal) temporal sequences of uncaged glutamate at spines has been demonstrated in cortical neurons in slices, but it is not clear what natural conditions would generate such sequences [38]. By contrast, single excitatory axonal inputs to MSO dendrites mediate a natural centripetal sequence of synaptic activity [15,28,39], and both current and previous modeling results highlight the importance of matching of input sequence conduction velocity with that of MSO dendrites, which conduct EPSPs at an average of ~0.3 ms^{-1}. In the present study, with the aid of 2-photon fluorescence-guided recordings we have been able to sample smaller diameter secondary and tertiary dendrites at longer distances from the soma. Our results reveal that the attenuation and delays of EPSPs propagating from these processes to the soma are more severe than previously estimated [40]. In our sample of modeled MSO neurons, these slower-conducting non-primary dendrites make up 70% of the surface area of the dendritic arbor in our sample of MSO neurons and thus play an outsized role in exerting temporal shifts in ITD curves in neurons with asymmetrical dendritic trees. These results emphasize that both branching and dendritic diameter are critical determinants of dendritic delay, as seen reflected in the morphoelectrotonic transforms (Fig. 5).

In the visual system, asymmetrical length and branching of the dendrites drives temporal disparities in the pattern of inhibition of ganglion cells, providing directional tuning to object movement [41–43]. The computation in the auditory system differs from vision in several fundamental ways. In the retina, spatial information is directly represented at the level of the photoreceptors, and tuning to spatial movement relies on the relative arrival times of excitatory and inhibitory inputs to the dendrites and soma. By contrast, in the cochlea space is not explicitly represented on the basilar membrane, which decomposes complex sounds spatially into different

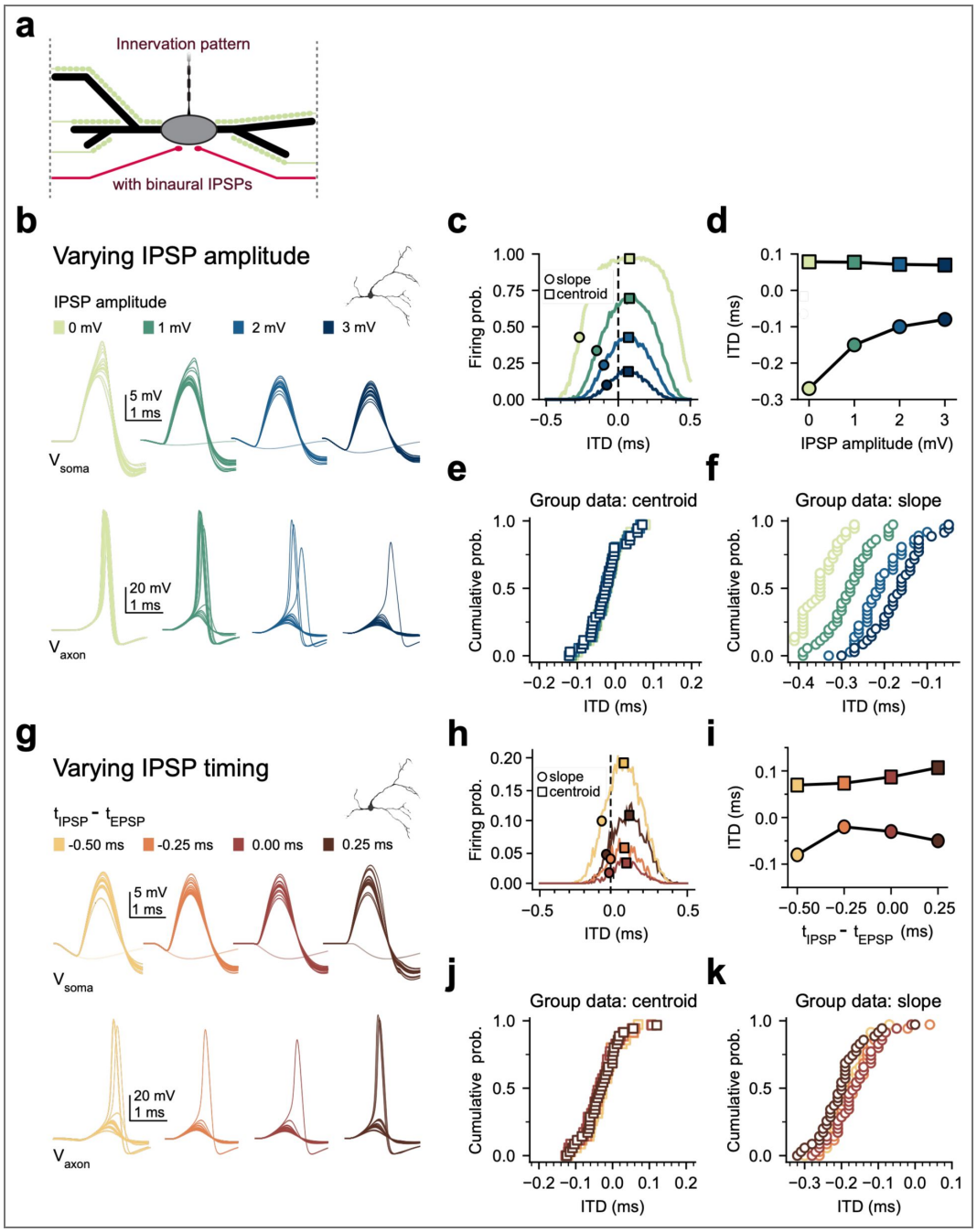

Fig. 7. Inhibition may serve to modulate a pre-established morphological baseline ITD response.

a, Schematic of innervation pattern with excitatory (green) and inhibitory (red) inputs. **b**, Somatic (top) and axonal (bottom) traces from ITD stimulation (ITD: 0.1 ms; IPSP timing: -0.5 ms) for each tested IPSP amplitude. Tested amplitude values and their unique colors above corresponding traces. Morphology of the exemplar neuron shown in the upper right. **c**, Exemplar cell's ITD response curves colored corresponding to IPSP amplitude in **b.** Centroid (square) and maximum slope (circle) are indicated for each curve. Dotted line at an ITD of zero. **d**, ITD centroid and maximum slope as a function of IPSP amplitude (colors corresponding to **b**). **e,f**, Group data (n=39) for ITD centroids (**e**) and steepest sections (**f**) for each IPSP amplitude. Data in **e** are largely overlapping. Shifting of population data in **f** corresponds to trend seen in the exemplar cell (**d**). **g-k**, Same as **b-f**, instead varying the timing of the inhibition (IPSP amplitude: 3 mV). Absolute firing probability, in **h**, is lower than **c**, resulting in lower signal to noise ratio. Centroids in **i** show more variation than **d**, though still minimal. Shift of exemplar cell's maximum slope ITD section (i) corresponds to degree of reduction in absolute firing probability (**h**).

frequency channels. Accordingly, horizontal spatial receptive fields must be constructed *de novo* in the MSO through the detection of synaptic binaural coincidence. In this way, ITDs serve as a proxy for horizontal position.

Other sources of asymmetry in binaural coincidence detection

Although our data reveal that the dendrites may contribute significant interaural delays in the binaural circuitry in the MSO, they likely work together with other mechanisms that have been proposed to influence binaural coincidence detection. In ~25% of MSO neurons in gerbils, the axon emerges from either the lateral or medial dendrites [44,45], and these results appear to extend to other mammalian species, including guinea pigs and cats [46,47]. Results from computer models suggest these offset axons, like asymmetrical dendrites, introduce strong asymmetries in synaptic integration and ITD tuning [48].

Inhibition has received considerable attention as a mechanism for ITD tuning based on shifts of tuning curves measured in single-unit recordings *in vivo* upon iontophoretic block of glycinergic synapses [18,19]. However, these results are controversial, as strong inhibition has not been observed in both juxtacellular and intracellular patch recordings *in vivo* [20,21,49], and there have been concerns about iontophoretic strychnine having off-target effects that alter both firing probability and input resistance [20]. We found that inhibition did not shift the overall location of ITD curves across the functional range of IPSP magnitudes (Fig. 7), consistent with pressure-applied strychnine data *in vivo* [20]. Inhibition shifted the location of maximal change in firing rate, consistent with a conventional "iceberg" model of inhibitory action on neuronal receptive fields. In mammals, the maximum rate of change, or slope of ITDs may be more important for population encoding of ITDs. Given that the maximal rising slope of firing invariably shifts toward 0 μs ITD when inhibition narrows ITD curves, both inhibition and dendritic asymmetry would both play key roles in setting the location of individual MSO neurons' receptive fields.

Comparison with avian binaural coincidence detectors

Binaural coincidence detection has been extensively studied in birds, and thus the comparison to mammals is noteworthy. Unlike mammals, dendritic morphology in bird MSO (nucleus laminaris) shows striking dependence on tonotopic location, exhibiting longer, more highly branched dendrites in neurons from low frequency regions [33,50]. While these tonotopic differences in dendritic length have garnered considerable attention, a close examination of dendritic parameters shows that nucleus laminaris neurons, like those in mammalian MSO, exhibit a continuum of dendritic asymmetry in the length of dendrites receiving ipsilateral and contralateral inputs (Smith and Rubel 1979, their Fig. 15 [33]). In these low frequency regions, inputs are restricted to distal, higher order branches [51]. Based on both our electrophysiological and modeling data, these higher order branches incur the largest delays as compared to the large-caliber primary dendrites and thus would be the primary determinants of dendritic propagation delay on each side. In the more highly specialized barn owls, the dendrites of laminaris neurons are more limited, and thus internal delay compensation must lie squarely on those provided by unmyelinated afferents [13].

Dendritic morphology and the scaling problem across species

The biological range of ITDs varies with head size [52,53], and thus any mechanism of internal delay must be scalable across species, accounting for ITDs differing by hundreds of microseconds (e.g., gerbil: ±130 μs [54], human: ± 600-700 μs [55]). A dendrite-based source of internal delay would be easily scalable, as the length of MSO dendrites increases with the size of different species. Although quantitative data are not available, previous morphological studies in guinea pig, ferret, cat and humans show that the dendritic arbors show considerable asymmetries [46,47,56,57].

Methods

All procedures were conducted in agreement with the Institutional Animal Care and Use Committee at The University of Texas at Austin (UT-Austin), which followed the guidelines of the National Institutes of Health. Mongolian gerbils (*Meriones unguiculatus*) were housed and raised in a colony at the UT-Austin Animal Resource Center. Animals experienced a 50/50 day/night cycle and had continuous access to food and water.

Brain slice preparation

both male and female gerbils (17-40 days old) were anesthetized with isoflurane and decapitated upon loss of the choroid reflex. The brain was removed from the cranium under warm (34-35°C) artificial cerebrospinal fluid (ACSF), the cerebellum was removed and the isolated hindbrain was glued to the stage of an oscillating tissue slicer (Leica VT-1200S). Horizontal sections were prepared at 200 µm thickness and stored at 35°C in a holding chamber for 45-60 min., and then gradually cooled to room temperature (24°C). All solutions were continuously bubbled with 95% O_2 / 5% CO_2. ACSF contained (in mM): 125 mM NaCl, 25 mM D-glucose, 2.5 mM KCl, 25 mM $NaHCO_3$, 1.25 mM NaH_2PO_4, 1.5mM $MgSO_4$, 1.5 mM $CaCl_2$, pH adjusted to 7.45 with NaOH, and final osmolarity at 315 mOsm.

Imaging and electrophysiological acquisition and analyses

neurons in the MSO were visualized under gradient contrast optics on a Leica TCS SP5 System equipped with a Coherent Chameleon Ultra II Ti:sapphire laser and an 8 kHz resonant scanner under control of Leica LAS AF Imaging Software. We found that gradient contrast images acquired via the photomultiplier tubes were of poor contrast in the heavily myelinated regions of the auditory brainstem, and so cell selection and seal formation was carried out under gradient contrast imaging through the epifluorescence port of the microscope and detected on a high-resolution monochrome digital camera (Zeiss Axiocam 503) running Zen software. The soma was recorded in whole-cell current clamp mode with a pipette (4 to 8 MΩ resistance) containing a potassium gluconate-based solution with 40-80 µM Alexa 594 added for visualizing cell morphology. After waiting ~10 min. for the dye to fill the dendritic arbor, a dendritic recording was made under 2-photon fluorescence with a second pipette (8 to 15 MΩ resistance) containing the same K Gluconate solution with 40-80 µM Alexa 488. Pipette solutions had a composition of 115 mM K-gluconate, 4.42 mM KCl, 0.5 mM EGTA, 10 mM HEPES, 10 mM, Na_2Phosphocreatine, 4 mM MgATP, and 0.3 mM NaGTP. Osmolality was adjusted to 300 mOsm/L with sucrose, and pH was adjusted to 7.30 with KOH. Seal resistances exceeded 1 GΩ, and recordings were discontinued if series resistances exceeded 20 or 50 MΩ for somatic and dendritic recordings, respectively.

Electrophysiological recordings were under the control of custom routines written in IGOR-Pro (Wavemetrics). Pipettes were prepared on a Sutter P-1000 puller using borosilicate glass (1.5 mm O.D.). Data was acquired using a pair of Dagan BVC-700, amplifiers in conjunction with an ITC-18 computer interface (Heka Instruments). Data was low-pass filtered at 5 kHz, sampled at 50 kHz, and stored on a Macintosh computer for further analyses using custom-written routines in IGOR-Pro.

Compartment model construction

A subpopulation of 40 fully intact reconstructed MSO neurons was selected from those gathered in Bondy et al. (2021) [34]. The reconstructed morphologies were imported into the NEURON simulation environment, using its Neurolucida importing tool. Computational compartments were created every 2 µm (Fig. S5a). Somatic and dendritic compartments were applied channel kinetics differentially, consisting of low and high-voltage-activated K channels [27,58], HCN channels[59], and leak channels, with sodium channels[60] exclusively in the somatic compartments. In simulations modeling a passive cell, high and low-voltage potassium and HCN channels were replaced with passive leak channels with conductances set to the average resting conductance of the preexisting active channels. In simulations with an axon, a model axon, with morphology as in

Lehnert (2014) [61], was attached at the center of the model soma. The axon channel kinetics implemented consisted of sodium channels, low-threshold potassium channels and leak channels in the nodes and initial segments, with solely leak channels in the internodes. Measurements from the axon were all recorded from the fifth node. Simulated synapses were conductance-based and shaped by an alpha function (τ = 290 μs).

Simulation variations

When measuring EPSP propagation, synapses were placed every 2 μm, with a unitary conductance that would maximally depolarize the soma 1 mV (unless noted otherwise). Each synapse was then stimulated and recorded separately. In ITD coincident detection procedures, dendrites were innervated with synapses (release probability=0.45) placed every 2 μm, totaling ~125 synapses for each side [62]. To mimic axonal activation, an artificial axonal input delay (Δt_{axon}) was calculated for each synapse as a function of conduction velocity (v_{input}) and axonal travel distance. The travel distance was considered zero at each side's furthest point from the soma. Otherwise, the axonal travel distance consists of two components: the mediolateral distance from the furthest point (Δt_{axon}=0) to the synapse's closest terminal segment; the path length from that terminal segment to the synapse (Fig. S5b). Artificial ITDs could then be added onto the calculated axonal delay. Each artificial ITD value (-0.5 to 0.5 ms, incremented by 0.01), was tested with 400 trials, and each trial consisted of a single stimulation of all synapses. To provide a more binary output, a model axon was attached to the cell's soma, and a spike was reported if a 25 mV depolarization from rest was recorded at the fifth and final axonal node. The synapses could then be adjusted with a unitary conductance to achieve an acceptable maximum firing probability. When implementing IPSP inputs to the ITD procedure, two inhibitory synapses were added at the soma, one corresponding to each mediolateral side. Each synapse generated an IPSP shaped by an alpha function with a time constant of 1.5 ms [62]. The timing of the synapses was adjusted relative to the artificial excitatory ITD signals. The amplitude of the IPSPs was adjusted by modifying the inhibitory synapses' conductances to achieve a combined IPSP hyperpolarization of approximately 1, 2, and 3 mV.

Data analyses

Measures of dendritic distance, both in slice experiments and in compartment models, were taken as the length along the dendritic arbor to the center of the somatic compartment. To address the variable size of the MSO within the slice plane, a normalized tonotopic location was calculated as the cell's distance from the most dorsal point of the MSO, relative to the entire MSO dorsoventral length. To provide a quantitative value of asymmetry between each cell's morphological measures, a unit of fold difference $\left(\log_2\left(\frac{\max\{\text{ medial, lateral }\}}{\min\{\text{ medial, lateral }\}}\right)+1\right)$ was used, with a value of 1 and 2 representing equal and double values, respectively. Average path length measurements were taken from the distances along the dendrite to the soma from each terminal section of the corresponding mediolateral arbor. Measurements for propagation attenuation and timing were taken at both the synaptic and somatic compartments of the model cell. For attenuation, the somatic depolarization for mediolateral sides was calculated by averaging each synaptic compartments propagated EPSP amplitude at the soma. Morpho-electrotonic transforms were created by scaling each sections length according to the natural logarithm of its attenuation $\left(\text{ section length }=\ln\left(\frac{V_{dend}}{V_{soma}}\right)\right)$. EPSP delay values were calculated by measuring the time between peak depolarization in the synaptic and somatic compartments. The corresponding delay transforms are scaled according to the delay contribution of each section. Mediolateral comparisons of delay were calculated by subtracting each sides average EPSP delay for all compartments. To minimize noise and data filtering for the ITD response, the centroid of the curve was measured, where half of the total area under the curve exists on either side. Comparisons were made using the absolute ITD centroid values to highlight the population of neurons' collective change. The ITD firing probabilities were smoothed with a Savitzky–Golay filter for the purpose of reasonably identifying the region of max slope for the curves.

Channel	Dendrite	Soma	TAIS	CAIS	Internode	Node
KLT (Mathews, 2010)	20	40	155	155		155
KHT (Nabel, 2019)	0.55	0.55				
HCN (Khurana, 2011)	1	1	2	2		
Na (Scott, 2010)	0	30	250	250		250
Leak	0.05	0.05	0.05	0.05	0.02	5

Table 1. Maximal channel conductances (μS/cm^2).

Tapered axon initial segment (TAIS) and constant disameter axon initial segment (CAIS).

Data availability

Data consist of both original physiological recordings as well as computational modeling. Modeling code can be accessed at the following repository: (*https://github.com/golding-lab/golding_mso* Powered

Additional files

Supplementary figures

Additional information

Funding

Funder	Grant reference number	Author
National Institute on Deafness and Other Communication Disorders (NIDCD)	NIH RO1 DC00788	Nace L Golding
National Institute on Deafness and Other Communication Disorders (NIDCD)	NIH F32 DC019534	Rebecca I Voglewede
National Institute on Deafness and Other Communication Disorders (NIDCD)	NIH F32 DC014890	Bradley Winters

Author ORCID iDs

Nace L Golding: https://orcid.org/0000-0003-4072-310X

References

1. **Grothe B.,** Pecka M (2014) The natural history of sound localization in mammals--a story of neuronal inhibition. *Front Neural Circuits* **8**:116 https://doi.org/10.3389/fncir.2014.00116 | PubMed
2. **Joris P.,** Yin T.C (2007) A matter of time: internal delays in binaural processing. *Trends Neurosci* **30**:70-78 https://doi.org/10.1016/j.tins.2006.12.004 | PubMed
3. **Carr C.E.,** Soares D., Parameshwaran S., Perney T (2001) Evolution and development of time coding systems. *Current Opinion in Neurobiology* **11**:727-733 https://doi.org/10.1016/s0959-4388(01)00276-8 | PubMed
4. **Stotler W.A** (1953) An experimental study of the cells and connections of the superior olivary complex of the cat. *J Comp Neurol* **98**:401-431 https://doi.org/10.1002/cne.900980303 | PubMed
5. **Lindsey B.G** (1975) Fine structure and distribution of axon terminals from the cochlear nucleus on neurons in the medial superior olivary nucleus of the cat. *J Comp Neurol* **160**:81-103 https://doi.org/10.1002/cne.901600106 | PubMed
6. **Yin T.C.,** Chan J.C (1990) Interaural time sensitivity in medial superior olive of cat. *J Neurophysiol* **64**:465-488 https://doi.org/10.1152/jn.1990.64.2.465 | PubMed
7. **Magnusson A.K.,** Kapfer C., Grothe B., Koch U (2005) Maturation of glycinergic inhibition in the gerbil medial superior olive after hearing onset. *J Physiol* **568**:497-512 https://doi.org/10.1113/jphysiol.2005.094763 | PubMed
8. **Kapfer C.,** Seidl A.H., Schweizer H., Grothe B (2002) Experience-dependent refinement of inhibitory inputs to auditory coincidence-detector neurons. *Nat Neurosci* **5**:247-253 https://doi.org/10.1038/nn810 | PubMed
9. **Spitzer M.W.,** Semple M.N (1995) Neurons sensitive to interaural phase disparity in gerbil superior olive: diverse monaural and temporal response properties. *J Neurophysiol* **73**:1668-1690 https://doi.org/10.1152/jn.1995.73.4.1668 | PubMed

10. **Goldberg J.M.,** Brown P.B (1969) Response of binaural neurons of dog superior olivary complex to dichotic tonal stimuli: some physiological mechanisms of sound localization. *J Neurophysiol* **32**:613-636 https://doi.org/10.1152/jn.1969.32.4.613 | PubMed

11. **Jeffress L.A** (1948) A place theory of sound localization. *J Comp Physiol Psychol* **41**:35-39 https://doi.org/10.1037/h0061495 | PubMed

12. **Carr C.E.,** Konishi M (1988) Axonal delay lines for time measurement in the owl's brainstem. *Proc Natl Acad Sci U S A* **85**:8311-8315 https://doi.org/10.1073/pnas.85.21.8311 | PubMed

13. **Carr C.,** Konishi M (1990) A circuit for detection of interaural time differences in the brain stem of the barn owl. *The Journal of neuroscience* https://doi.org/10.1523/jneurosci.10-10-03227.1990 | PubMed

14. **Moiseff A.,** Konishi M (1981) Neuronal and behavioral sensitivity to binaural time differences in the owl. *J Neurosci* **1**:40-48 https://doi.org/10.1523/jneurosci.01-01-00040.1981 | PubMed

15. **Beckius G.E.,** Batra R., Oliver D.L (1999) Axons from anteroventral cochlear nucleus that terminate in medial superior olive of cat: observations related to delay lines. *J Neurosci* **19**:3146-3161 https://doi.org/10.1523/jneurosci.19-08-03146.1999 | PubMed

16. **Smith P.H.,** Joris P.X., Carney L.H., Yin T.C (1991) Projections of physiologically characterized globular bushy cell axons from the cochlear nucleus of the cat. *J Comp Neurol* **304**:387-407 https://doi.org/10.1002/cne.903040305 | PubMed

17. **Myoga M.H.,** Lehnert S., Leibold C., Felmy F., Grothe B (2014) Glycinergic inhibition tunes coincidence detection in the auditory brainstem. *Nat Commun* **5**:3790 https://doi.org/10.1038/ncomms4790 | PubMed

18. **Pecka M.,** Brand A., Behrend O., Grothe B (2008) Interaural time difference processing in the mammalian medial superior olive: the role of glycinergic inhibition. *J Neurosci* **28**:6914-6925 https://doi.org/10.1523/jneurosci.1660-08.2008 | PubMed

19. **Brand A.,** Behrend O., Marquardt T., McAlpine D., Grothe B (2002) Precise inhibition is essential for microsecond interaural time difference coding. *Nature* **417**:543-547 https://doi.org/10.1038/417543a | PubMed

20. **Franken T.P.,** Roberts M.T., Wei L., Golding N.L., Joris P.X (2015) In vivo coincidence detection in mammalian sound localization generates phase delays. *Nat Neurosci* **18**:444-452 https://doi.org/10.1038/nn.3948 | PubMed

21. **Roberts M.T.,** Seeman S.C., Golding N.L (2013) A mechanistic understanding of the role of feedforward inhibition in the mammalian sound localization circuitry. *Neuron* **78**:923-935 https://doi.org/10.1016/j.neuron.2013.04.022 | PubMed

22. **Heijden M. van der,** Lorteije J.A., Plauska A., Roberts M.T., Golding N.L., Borst J.G (2013) Directional hearing by linear summation of binaural inputs at the medial superior olive. *Neuron* **78**:936-948 https://doi.org/10.1016/j.neuron.2013.04.028 | PubMed

23. **Jercog P.E.,** Svirskis G., Kotak V.C., Sanes D.H., Rinzel J (2010) Asymmetric excitatory synaptic dynamics underlie interaural time difference processing in the auditory system. *PLoS Biol* **8**:e1000406 https://doi.org/10.1371/journal.pbio.1000406 | PubMed

24. **Shamma S.A.,** Shen N., Gopalaswamy P (1989) Stereausis: binaural processing without neural delays. *The Journal of the Acoustical Society of America* **86**:989-1006 https://doi.org/10.1121/1.398734 | PubMed

25. **Plauška A.,** Heijden M.V.D., Borst J.G.G (2017) A test of the stereausis hypothesis for sound localization in mammals. *Journal of Neuroscience* **37**:7278-7289 https://doi.org/10.1523/jneurosci.0233-17.2017 | PubMed

26. **Agmon-Snir H.,** Carr C.E., Rinzel J (1998) The role of dendrites in auditory coincidence detection. *Nature* **393**:268-272 https://doi.org/10.1038/30505 | PubMed

27. **Mathews P.J.,** Jercog P.E., Rinzel J., Scott L.L., Golding N.L (2010) Control of submillisecond synaptic timing in binaural coincidence detectors by K(v)1 channels. *Nat Neurosci* **13**:601-609 https://doi.org/10.1038/nn.2530 | PubMed

28. **Callan A.R.,** Hess M., Felmy F., Leibold C (2021) Arrangement of Excitatory Synaptic Inputs on Dendrites of the Medial Superior Olive. *J Neurosci* **41**:269-283 https://doi.org/10.1523/jneurosci.1055-20.2020 | PubMed

29. **Franken T.P.,** Bremen P., Joris P.X (2014) Coincidence detection in the medial superior olive: Mechanistic implications of an analysis of input spiking patterns. *Frontiers in Neural Circuits* **8**:42 https://doi.org/10.3389/fncir.2014.00042 | PubMed

30. **Dasika V.K.,** White J.A., Colburn H.S (2007) Simple models show the general advantages of dendrites in coincidence detection. *J Neurophysiol* **97**:3449-3459 https://doi.org/10.1152/jn.00669.2005 | PubMed

31. **Feng A.S.,** Rogowski B.A (1980) Effects of monaural and binaural occlusion on the morphology of neurons in the medial superior olivary nucleus of the rat. *Brain Research* **189**:530-534 https://doi.org/10.1016/0006-8993(80)90112-2 | PubMed

32. **Russell F.A.,** Moore D.R (1999) Effects of unilateral cochlear removal on dendrites in the gerbil medial superior olivary nucleus. *Eur J Neurosci* **11**:1379-1390 https://doi.org/10.1046/j.1460-9568.1999.00547.x | PubMed

33. **Smith D.J.,** Rubel E.W (1979) Organization and development of brain stem auditory nuclei of the chicken: dendritic gradients in nucleus laminaris. *J Comp Neurol* **186**:213-239 https://doi.org/10.1002/cne.901860207 | PubMed

34. **Bondy B.J.,** Haimes D.B., Golding N.L (2021) Physiological diversity influences detection of stimulus envelope and fine structure in neurons of the medial superior olive. *J Neurosci* https://doi.org/10.1523/jneurosci.2354-20.2021 | PubMed

35. **Hoffmeister B.,** Jänig W., Lisney S.J.W (1991) A proposed relationship between circumference and conduction velocity of unmyelinated axons from normal and regenerated cat hindlimb cutaneous nerves. *Neuroscience* **42**:603-611 https://doi.org/10.1016/0306-4522(91)90402-a | PubMed

36. **Werthat F.,** Alexandrova O., Grothe B., Koch U (2008) Experience-dependent refinement of the inhibitory axons projecting to the medial superior olive. *Dev Neurobiol* **68**:1454-1462 https://doi.org/10.1002/dneu.20660 | PubMed

37. **Rinzel J.,** Rall W (1974) Transient response in a dendritic neuron model for current injected at one branch. *Biophys J* **14**:759-790 https://doi.org/10.1016/s0006-3495(74)85948-5 | PubMed

38. **Branco T.,** Clark B.A., Häusser M (2010) Dendritic discrimination of temporal input sequences in cortical neurons. *Science* **329**:1671-1675 https://doi.org/10.1126/science.1189664 | PubMed

39. **Smith P.H.,** Joris P.X., Yin T.C (1993) Projections of physiologically characterized spherical bushy cell axons from the cochlear nucleus of the cat: evidence for delay lines to the medial superior olive. *J Comp Neurol* **331**:245-260 https://doi.org/10.1002/cne.903310208 | PubMed

40. **Winters B.D.,** Jin S.X., Ledford K.R., Golding N.L (2017) Amplitude Normalization of Dendritic EPSPs at the Soma of Binaural Coincidence Detector Neurons of the Medial Superior Olive. *J Neurosci* **37**:3138-3149 https://doi.org/10.1523/jneurosci.3110-16.2017 | PubMed

41. **Bloomfield S.A** (1994) Orientation-sensitive amacrine and ganglion cells in the rabbit retina. *Journal of Neurophysiology* **71**:1672-1691 https://doi.org/10.1152/jn.1994.71.5.1672 | PubMed

42. **Trenholm S.,** Johnson K., Li X., Smith R.G., Awatramani G.B (2011) Parallel mechanisms encode direction in the retina. *Neuron* **71**:683-694 https://doi.org/10.1016/j.neuron.2011.06.020 | PubMed

43. **Bloomfield S.A** (1991) Two types of orientation-sensitive responses of amacrine cells in the mammalian retina. *Nature* **350**:347-350 https://doi.org/10.1038/350347a0 | PubMed

44. **Scott L.L.,** Mathews P.J., Golding N.L (2005) Posthearing developmental refinement of temporal processing in principal neurons of the medial superior olive. *J Neurosci* **25**:7887-7895 https://doi.org/10.1523/jneurosci.1016-05.2005 | PubMed

45. **Rautenberg P.L.,** Grothe B., Felmy F (2009) Quantification of the three-dimensional morphology of coincidence detector neurons in the medial superior olive of gerbils during late postnatal development. *J Comp Neurol* **517**:385-396 https://doi.org/10.1002/cne.22166 | PubMed

46. **Cajal S.R.Y** (1907) Structure et connexions des neurones. *Nordiskt Medicinskt Arkiv* **40**:1-28 https://doi.org/10.1111/j.0954-6820.1907.tb00034.x

47. **Smith P.H** (1995) Structural and functional differences distinguish principal from nonprincipal cells in the guinea pig MSO slice. *J. Neurophysiol* **73**:1653-1667 https://doi.org/10.1152/jn.1995.73.4.1653 | PubMed

48. **Zhou Y.,** Carney L.H., Colburn H.S (2005) A model for interaural time difference sensitivity in the medial superior olive: interaction of excitatory and inhibitory synaptic inputs, channel dynamics, and cellular morphology. *J Neurosci* **25**:3046-3058 https://doi.org/10.1523/jneurosci.3064-04.2005 | PubMed

49. **Plauska A.,** Borst J.G., Heijden M. van der (2016) Predicting binaural responses from monaural responses in the gerbil medial superior olive. *J Neurophysiol* **115**:jn.01146.2015 https://doi.org/10.1152/jn.01146.2015 | PubMed

50. **Wang Y.,** Rubel E.W (2008) Rapid regulation of microtubule-associated protein 2 in dendrites of nucleus laminaris of the chick following deprivation of afferent activity. *Neuroscience* **154**:381-389 https://doi.org/10.1016/j.neuroscience.2008.02.032 | PubMed

51. **Yamada R.,** Kuba H (2021) Dendritic synapse geometry optimizes binaural computation in a sound localization circuit. *Science Advances* **7** https://doi.org/10.1126/sciadv.abh0024 | PubMed

52. **Jones H.G.,** Koka K., Thornton J.L., Tollin D.J (2011) Concurrent development of the head and pinnae and the acoustical cues to sound location in a precocious species, the chinchilla (Chinchilla lanigera). *J Assoc Res Otolaryngol* **12**:127-140 https://doi.org/10.1007/s10162-010-0242-3 | PubMed

53. **Koka K.,** Jones H.G., Thornton J.L., Lupo J.E., Tollin D.J (2011) Sound pressure transformations by the head and pinnae of the adult Chinchilla (Chinchilla lanigera). *Hear Res* **272**:135-147 https://doi.org/10.1016/j.heares.2010.10.007 | PubMed

54. **Maier J.K.,** Klump G.M (2006) Resolution in azimuth sound localization in the Mongolian gerbil (Meriones unguiculatus). *The Journal of the Acoustical Society of America* **119**:1029-1036 https://doi.org/10.1121/1.2159429 | PubMed

55. **George K** (1977) Model for the intramural time differences in the azimuthal plane. *J. Acoust. Soc. Am* **62**:157-167 https://doi.org/10.1121/1.381498

56. **Henkel C.K.,** Brunso-Bechtold J.K (1990) Dendritic morphology and development in the ferret medial superior olivary nucleus. *J Comp Neurol* **294**:377-388 https://doi.org/10.1002/cne.902940307 | PubMed

57. **Kulesza R** (2008) Cytoarchitecture of the human superior olivary complex: nuclei of the trapezoid body and posterior tier. *Hear Res* **241**:52-63 https://doi.org/10.1016/j.heares.2008.04.010 | PubMed

58. **Nabel A.L.,** Callan A.R., Gleiss S.A., Kladisios N., Leibold C., Felmy F (2019) Distinct distribution patterns of potassium channel sub-units in somato-dendritic compartments of neurons of the medial superior olive. *Frontiers in Cellular Neuroscience* **13**:409471 https://doi.org/10.3389/fncel.2019.00038

59. **Khurana S.,** Liu Z., Lewis A.S., Rosa K., Chetkovich D., Golding N.L (2012) An essential role for modulation of hyperpolarization-activated current in the development of binaural temporal precision. *J Neurosci* **32**:2814-2823 https://doi.org/10.1523/jneurosci.3882-11.2012 | PubMed

60. **Scott L.L.,** Mathews P.J., Golding N.L (2010) Perisomatic voltage-gated sodium channels actively maintain linear synaptic integration in principal neurons of the medial superior olive. *J Neurosci* **30**:2039-2050 https://doi.org/10.1523/jneurosci.2385-09.2010 | PubMed

61. **Lehnert S.,** Ford M.C., Alexandrova O., Hellmundt F., Felmy F., Grothe B., Leibold C (2014) Action potential generation in an anatomically constrained model of medial superior olive axons. *J Neurosci* **34**:5370-5384 https://doi.org/10.1523/jneurosci.4038-13.2014 | PubMed

62. **Couchman K.,** Grothe B., Felmy F (2010) Medial superior olivary neurons receive surprisingly few excitatory and inhibitory inputs with balanced strength and short-term dynamics. *J Neurosci* **30**:17111-17121 https://doi.org/10.1523/jneurosci.1760-10.2010 | PubMed

Peer reviews

Reviewer #1 (Public review):

Overview:

This study examines cellular computations in the dendrites of neurons in the medial superior olive (MSO) required for computing sound location based on interaural time differences (ITD). This field had, for many decades, depended on the so-called Jeffress model, which stated that an array of binaural coincidence detector neurons fire only when a given sound lateralization is balanced by a given difference in presynaptic axonal conduction time. The apparent absence of such calibrated axonal delay lines has left the field with little mechanistic handle for the strong ITD computations in MSO. This study suggests that dendritic delay along the dendrites of the bipolar MSO neurons makes a significant contribution to a calibrated delay line.

Strengths:

The authors used a combination of in vitro patch-clamp recordings, morphological analysis of a large dataset, and computational modelling to gain experimental access to dendritic computations. A technical tour-de-force set of distal dendritic patch-clamp recordings allowed an evaluation of this otherwise inaccessible parameter, and detailed modeling based on large datasets revealed the functional consequences. The use of this broad methodological toolbox enabled a detailed study of dendritic integration in MSO neurons and revealed a prominent role for graded variation in dendrite structure in shaping the coincidence detection in MSO neurons. In addition, the modeled effects of synaptic inhibition were quite striking and shaped our understanding of ITD coding in the MSO.

Weaknesses:

The paper's organization does not set up the reader very well for the major point to be made about exactly how dendritic asymmetry could bias ITD curves. This point only arises later in the paper after discussion of uncorrelated physiological measures that merely hint that what is important is "larger morphological and electrotonic structure". The paper could also benefit from a more complete description of the methodology. As an example, bridge balance goes unmentioned, and series resistance is hardly mentioned, even though both could distort the measurements of simulated EPSP amplitudes made through tiny electrodes used for dendrite recording.

https://doi.org/10.7554/eLife.111364.1.sa3

Reviewer #2 (Public review):

Medial superior olivary neurons are sensitive to interaural time differences in the microsecond range, and many cellular mechanisms have been advanced to explain this temporal sensitivity. This study provides experimental and computational evidence for a new mechanism in which a range of asymmetric dendritic delays permits individual MSO neurons to represent the full range of biologically relevant ITDs. Using elegant 2-photon guided simultaneous recordings from distal dendrite and soma, along with compartmental modeling on anatomically reconstructed neurons, the authors provide compelling evidence that this mechanism contributes to microsecond-level tuning. The experimental design, analyses, and narrative are all well-crafted. It's a beautiful study. As outlined below, I have two general questions about interpretations drawn from the experimental data and modeling.

(1) Both excitatory and inhibitory synapses on MSO neurons display significant short-term depression (Couchman et al., 2010). Given the amount of attenuation at the soma, the role that the distal inputs would play after stimulus onset has not been tested. Were simulated EPSC pulse trains with endogenous short-term plasticity kinetics injected into distal dendrites? If not, were EPSP and IPSP trains with endogenous short-term plasticity kinetics studied in the model? The fundamental question is how much distal synapses contribute to somatic spike initiation as a function of synaptic pulse number.

(2) The model provides a credible line of evidence that synaptic inputs from distal and tertiary compartments can generate reliable increases in the time of arrival at the soma. It would be relatively simple to sequentially prune dendritic compartments to address how the time difference at which the maximal firing rate scales with tertiary or distal compartments. Similarly, one could eliminate the primary dendrites to determine whether or not they play a functional role. I would expect these chores to be largely confirmatory, but since EPSP delay and amplitude are convolved, it would increase confidence in the interpretation.

(3) Two technical questions. The age range is fairly broad, and it is not clear at which ages the experimental recordings were obtained, especially for the key experimental graphs that show correlations between delay (Figure 1d) or tau (Figure 2e) and distance. In addition, age could be added to Supplementary Figure 1, and the data could be ordered from youngest to oldest. Second, the Methods section indicates that brain slices were gradually cooled to 25 {degree sign}C, but should specify whether or not the recordings were obtained at this temperature.

https://doi.org/10.7554/eLife.111364.1.sa2

Reviewer #3 (Public review):

Summary:

The study addresses how mammalian medial superior olive (MSO) neurons generate the internal delays required for interaural time difference (ITD) coding and sound localization. The authors demonstrate that dendritic morphology, particularly asymmetry between lateral and medial dendritic arbors, contributes to differential EPSP propagation delays and thereby shifts the optimal ITD of individual MSO neurons, using two-photon-guided paired dendritic and somatic recordings with compartmental modeling. This is a strong and potentially impactful manuscript. The work provides compelling evidence that dendritic morphology contributes to coincidence detection and ITD tuning in MSO neurons.

Strengths:

A major strength of the study is its technically rigorous combination of experimental electrophysiology, detailed neuronal reconstructions, and computational modeling. The use of paired dendritic and somatic recordings provides direct physiological insight into EPSP propagation, while the modeling approach allows the authors to test how cell-specific morphology influences coincidence detection. The analysis of multiple reconstructed MSO neurons further supports that dendritic asymmetry generates differential EPSP propagation delays that contribute to ITD tuning. This is a novel and potentially important mechanism that may complement classical axonal delay-line models. The study is strong in its anatomical and electrophysiological approach.

Weaknesses:

No major weakness. However, some aspects of the methods and interpretation would benefit from clarification. First, the assumptions used in the compartmental models should be more explicitly described, including the distribution of glutamatergic synaptic inputs and synaptic conductance parameters. It would be useful to clarify whether excitatory inputs were

assumed to be homogeneously distributed along primary and higher-order dendritic branches or assigned based on known MSO input organization. Anatomical validation using VGluT staining together with dendritic labeling could strengthen the physiological relevance of the modeled input patterns. Second, the morphological analysis is informative, but additional measures of dendritic complexity could further support the conclusions. In addition to path length and membrane surface area, analyses of primary neurite number, branch points, and terminal arbors, using Sholl profiles or fractal dimension, could provide a more comprehensive assessment of lateral-medial dendritic asymmetry.

https://doi.org/10.7554/eLife.111364.1.sa1

Author response:

We thank the reviewers for their enthusiasm for the work as well as for their thoughtful and constructive comments, which will lead to many improvements in the manuscript. We will address their concerns/suggestions in the following ways:

Reviewer 1

(1) We will revise text to help the reader more intuitively understand how dendritic asymmetry can translate into alterations in receptive field location, as well as provide a better description of the cited portions of the Methods section.

Reviewer 2

(1) The simulations in the current version of the manuscript modeled a transient response via a single synaptic conductance in part because one can better visualize the interplay between synaptic inputs and voltage-gated ion channels across both time and dendritic space. However, we agree that it is also important to show how our results are impacted during ongoing trains of synaptic activity exhibiting short-term depression as documented in the literature. We will add an additional figure showing simulations employing realistic statistical patterns of presynaptic excitatory and inhibitory inputs with appropriate short-term plasticity characteristics. These simulations are already complete and show that the increased complexity minimally alters the location of modeled ITD curves of the cell population over a wide range of frequencies (250 Hz – 2 kHz).

(2) The reviewer's suggestion of sequentially pruning the different orders of dendritic branches is an excellent one. However, removal of dendrites also alters overall whole cell resistance and capacitance as well as the cable properties of the remaining dendrites. It is thus impossible to disentangle the branch-specific effects of synapse location from changing intrinsic electrical properties. However, the reviewer has inspired us to address their suggestion in a slightly different way: we will add (via a new figure) simulations that take place in the same dendritic arbor, but with inputs restricted to progressively lower orders of dendritic branches. Thus, the relative contributions of synapses onto higher order dendritic branches can be visualized without fundamentally changing the electrotonic structure of the simulated neurons across the different conditions. These simulations will be performed under the "*in vivo*-like" conditions described in the previous point. We think they will effectively address the essence of the reviewer's suggestion.

(3) We will add more specific information about animal ages in relevant figures, including Supplementary Figure 1. We will also indicate that all physiological recordings were performed near physiological temperature (35°C), which was unintentionally omitted.

Reviewer 3

(1) We will add more detail about the anatomical assumptions regarding spatial input patterns vs. higher order dendrites. We do not think that VGluT staining with dendritic

labeling will be a productive experiment, since the thin sections that provide high quality labeling conditions also preclude following single dendrites for long distances. The distal portions, which are of particular interest, are most difficult to follow because of their smaller diameter and more extensive branching out of the plane of thin sections. Further, the work of Callan and colleagues (2021) has addressed axonal input patterns as well as dendritic coverage, documenting that single axon inputs follow dendrites for variable distances, and typically provide multiple synaptic contacts. This work also highlights the many challenges and large effort involved in documenting synaptic innervation patterns in single cells at the light microscopic level. Thus, we do not think we can improve upon existing anatomical descriptions without excessively expanding the scope of an already long study, which will have 9 figures after revision.

(2) We have analyzed many other measures of dendritic complexity but for reasons of clarity and focus included the two measures that appeared most intuitive and impactful (length and surface area). We agree that access to other measures would be useful even if some are less intuitive, and thus we will provide a more comprehensive analysis of dendritic structure in a supplementary figure.

References:

Callan, A. R., Heß, M., Felmy, F., & Leibold, C. (2021). Arrangement of Excitatory Synaptic Inputs on Dendrites of the Medial Superior Olive. The Journal of neuroscience, 41(2), 269–283. *https://doi.org/10.1523/JNEUROSCI.1055-20.2020*

https://doi.org/10.7554/eLife.111364.1.sa0